Computer Methods and Programs in Biomedicine 245 (2024) 108034

Contents lists available at ScienceDirect

Computer Methods and Programs in Biomedicine

journal homepage: www.elsevier.com/locate/cmpb

A novel mono-physics particle-based approach for the simulation of cardiovascular fluid-structure interaction problems

Alessandra Monteleone [a], Sofia Di Leonardo [a], Enrico Napoli [b], Gaetano Burriesci [a,c,*]

[a] Ri.MED Foundation, Palermo, Italy
[b] Engineering Department, University of Palermo, Italy
[c] UCL Mechanical Engineering, University College London, UK

ARTICLE INFO

Keywords:
Smoothed particle hydrodynamics (SPH)
Fluid-structure interaction (FSI)
Particle-spring system
Aortic valve dynamics
Cardiovascular numerical simulation

ABSTRACT

Background and objective: Fluid-structure interaction (FSI) is required in the study of several cardiovascular engineering problems were the mutual interaction between the pulsatile blood flow and the tissue structures is essential to establish the biomechanics of the system. Traditional FSI methods are partitioned approaches where two independent solvers, one for the fluid and one for the structure, are asynchronously coupled. This process results into high computational costs. In this work, a new FSI scheme which avoids the coupling of different solvers is presented in the framework of the truly incompressible smoothed particle hydrodynamics (ISPH) method.

Methods: In the proposed FSI method, ISPH particles contribute to define both the fluid and structural domains and are solved together in a unified system. Solid particles, geometrically defined at the beginning of the simulation, are linked through spring bounds with elastic constant providing the material Young's modulus. At each iteration, internal elastic forces are calculated to restore the springs resting length. These forces are added in the predictor step of the fractional-step procedure used to solve the momentum and continuity equations for incompressible flows of all particles.

Results: The method was validated with a benchmark test case consisting of a flexible beam immersed in a channel. Results showed good agreement with the system coupling approach of a well-established commercial software, ANSYS®, both in terms of fluid-dynamics and beam deformation. The approach was then applied to model a complex cardiovascular problem, consisting in the aortic valve operating function. The valve dynamics during opening and closing phases were compared qualitatively with literature results, demonstrating good consistency.

Conclusions: The method is computationally more efficient than traditional FSI strategies, and overcomes some of their main drawbacks, such as the impossibility of simulating the correct valve coaptation during the closing phase. Thanks to the incompressibility scheme, the proposed FSI method is appropriate to model biological soft tissues. The simplicity and flexibility of the approach also makes it suitable to be expanded for the modelling of thromboembolic phenomena.

1. Introduction

A number of engineering phenomena are the result of the mutual interaction between fluid fields and solid bodies, where the solid bodies deform as effect of the load exerted by the fluid and the resulting displacement of the structure affects the fluid flow [1,2]. This two-way fluid-structure interaction (FSI) is crucial in the modelling of cardiovascular problems, such as the dynamics of heart valves, where the mutual interaction of highly deformable soft tissues with pulsatile blood flows determines the correct physiological functions, and its alterations result into pathological conditions [3–5]. In this context, computational FSI methods have established as essential tools to simulate operating conditions and analyse the system biomechanics, improving the understanding of complex pathophysiology and supporting the development of advanced clinical treatments [6,7]. In fact, despite their higher numerical complexity, FSI approaches are substantially more accurate when compared with the single solution for computational fluid and structural dynamics methods (CFD and CSD, respectively) [8]; and

* Corresponding author at: Room 507A, Malet Place Engineering Building, Torrington Place, London, WC1E 7JE.
E-mail address: g.burriesci@ucl.ac.uk (G. Burriesci).

https://doi.org/10.1016/j.cmpb.2024.108034
Received 16 November 2023; Received in revised form 9 January 2024; Accepted 14 January 2024
Available online 15 January 2024

become necessary when studying phenomena where the wall shear stress distribution and profiles are important [9].

Several FSI approaches were proposed in the past [4,8,10], which are generally classified as partitioned and monolithic approaches [10]. In partitioned approaches the fluid and structure solutions are obtained from separate well-established methods, independently implemented for the analysis of fluid dynamics and structural problems, that are asynchronously coupled at the fluid-structure interface. On the contrary, in monolithic FSI approaches both fluid and structure governing equations are solved simultaneously by a unified matrix, automatically satisfying the conditions at the interface in the solution procedure. Partitioned approaches allow software modularity, since the most suitable solver can be selected for each domain and no mesh matching is required at the fluid-structure interface. On the other hand, monolithic approaches are computationally more robust and efficient than the partitioned counterparts [11–14].

Traditionally, fluid flows are modelled using the Eulerian description, whilst the Lagrangian formulation is long-established for structural analyses. Hence, appropriate strategies are implemented to combine the two formulations. In this framework, *arbitrary Lagrangian Eulerian* (ALE) [15–18] and *immersed boundary* (IB) [19–26] techniques are commonly used, which broadly differ for the discretisation of the fluid domain. In ALE approaches, originally proposed by Donea et al. [15], the fluid mesh can deform following the movement of the structure, thus providing a robust fluid-structure coupling. However, when large deformations of the structure occur, the remeshing of the fluid domain, essential to avoid severe distortion of the mesh elements, results in an increase in complexity and computational costs of the simulation [27]. Moreover, additional specialised algorithms must be introduced when simulating phenomena where the fluid domain can be partitioned into two unconnected regions. Typically, in these cases a minimum threshold distance needs to be imposed between the structure walls that would physically get in contact, so as to preserve continuity of the fluid domain during the whole simulation [8,28] and to prevent highly distorted meshes [29]. This is a limitation in the simulation of a number of biomechanical problems, such as peristaltic phenomena or cardiac/venous valves functioning, as it introduces artefactual leakage.

The IB method was specifically introduced by Peskin [19] to simulate flow patterns around heart valves, and then widespread for modelling fluid-structure interaction problems in other fields [21]. In this approach, the fluid mesh is fixed, whilst the mesh of the structure is free to deform. Since only the mesh of the structure deforms and no fluid mesh refinement is required at the fluid-structure interface, IB approaches have lower computational cost than ALE, and there are no issues related to ill-shaped elements of the fluid mesh. As a result, this method is usually preferred for FSI problems characterised by large deformations of immersed thin structures, such as for modelling heart valve dynamics [23]. Still, as in ALE approaches, a small gap of fluid cells around the immersed structures is required to allow structures' separation. Therefore, achieving correct solid contact still remains unresolved [30,31]. Moreover, since variables are obtained from interpolation rather than calculated, results at the fluid-structure interface are less accurate than with ALE approaches.

Other FSI strategies are based on the fictious domain method, where Eulerian and Lagrangian formulations are employed for the fluid and solid, respectively, and Lagrange multipliers are used to enforce the kinematic condition associated to the moving internal boundaries [25,32,33]. Hsu et al. [34] presented a hybrid ALE/immersed-boundary technique to simulate a bioprosthetic heart valve implanted in a deformable artery.

In this context, fully Lagrangian FSI approaches have been proposed, which lead to a strong coupling between the structure and the fluid. Khayyer et al. [35] highlight the potential robustness of these advanced solvers, which are particularly suitable for large deformation problems [36–38]. In particular, particle-based FSI schemes using the smoothed particle hydrodynamics (SPH) method are common choices [39–41]. SPH was originally introduced by Lucy [42] and Gingold & Monahan [43] in astrophysics, and then expanded to several fields of engineering and science [44,45], including FSI modelling [46,47]. Several partitioned FSI schemes are based on coupling SPH, which is used for the fluid modelling, with the accurate and robust finite element (FE) method, employed for the structure dynamics [48]. Fourey et al. [49] proposed this type of coupling to model violent FSI problems involving complex free surface flows with deformable structures. Long et al. [50] proposed a new ghost particle method to couple FE with SPH. Fuchs et al. [51] presented a novel SPH-FE formulation with sliding boundary particles, aiming to achieve an accurate representation of the interaction forces between fluid particles and structural elements. In the cardiovascular area, Mao et al. [27] used a fully-coupled FSI combining SPH and FE to investigate the aortic and mitral valves structural response and the intraventricular hemodynamics in a realistic left ventricle model. Dabiri et al. [52] used SPH coupled with FE to simulate the blood flow through the tricuspid valve, with and without the MitraClip intervention, aiming at evaluating the procedure impact over tricuspid regurgitation. McLoone and Quinlan [53] coupled a mesh-less finite volume particle method and FE to simulate thin elastic structures, applying the method to a 2D simulation of an idealised heart valve leaflet. SPH was also coupled with the element bending group method [54,55]. Zhang et al. [56] proposed a FSI approach where SPH is coupled with a smoothed finite element method. This FSI approach was further improved by Zhang et al. [57] introducing multi-resolution SPH to simulate complex hydroelastic FSI problems. Shimizu et al. [58] presented an enhanced particle-based FSI scheme coupling a truly-incompressible SPH (ISPH) fluid model with a purely Lagrangian meshfree hydroelastic FSI solver, which allows consistent fluid–structure time coupling adopting the equivalent time step sizes in both phases. Zhang et al. [59,60] combined SPH-based approaches with smoothed point interpolation method, where the coupling is achieved by introducing ghost and repulsive particles at the interface to recover the continuity of the support domain and prevent particle penetration into structural subdomain. Rahimi et al., 2022 proposed a different FSI approach that couples SPH with the Peridynamic mesh-free method, enabling structural damage modelling and tracking [61].

SPH was also used to analyse computational solid mechanics problems [62–64] and, in FSI approaches, to describe both fluid and solid domains, using the weakly-compressible (WCSPH) [65,66] and the ISPH [67,68] techniques. Zhan et al. [69] implemented an approach coupling the total Lagrangian and WCSPH method to model 3D FSI problems. Khayyer et al. [68] developed an enhanced ISPH-SPH method where structure particles are considered as moving wall boundaries for the fluid, providing velocity and position boundary conditions in calculation of the pressure field. This scheme was further improved in Khayyer et al. [70], where ISPH is used to model fluid flows and Hamiltonian SPH is employed for the description of laminated composite elastic structures. Sun et al. [71] developed an FSI-SPH model by combining the multi-resolution δ+-SPH scheme and a Total Lagrangian SPH method to model complex 3D FSI problems. O'Connor et al. [72] proposed a GPU-accelerated SPH method to model FSI problems involving violent hydrodynamics of free-surface flows interacting with flexible structures.

SPH was also coupled with the discrete element method for the solid phase, where particles are typically connected via spring-like forces [73,74]. Ariane et al. [75] developed a fully Lagrangian discrete multi-physics model to simulate the dynamics of free emboli in double venous valve systems with flexible walls. Within the context of lattice spring models [76], several FSI models based on SPH have been proposed in literature to simulate large deformation problems [77–81]. Recently, Monteleone et al. [82] proposed a partitioned 3D FSI approach, where the ISPH method is employed to simulate the motion of incompressible fluid flows, whilst a particle–spring systems solver is used for the structure description.

In the present work, a novel FSI approach is presented, which overcomes the main drawbacks of traditional FSI strategies in the

modelling of cardiovascular problems. The model, fully integrated in the ISPH framework, is implemented in the code PANORMUS (PArallel Numerical Open-souRce Model for Unsteady flow Simulations) [83].

The method involves the representation of both fluid and solid domains by SPH particles and, in contrast with partitioned methods, employs a single algorithm to solve the two domains. Moreover, differently from monolithic approaches, a single physics is employed. This is possible thanks to the fact that biological soft tissues exhibit incompressibility and similar density to the fluid they interact with [8,84–87]. In order to simulate the structural behaviour, the particles representing the solid domain are bounded to each other via spring links. The spring constant is calibrated through a basic relationship to describe the Young's modulus of the material.

The proposed method exploits the mesh-less features of SPH to model FSI coupling without interfaces, domains with complex geometries and challenging structural contact problems. The strength of the presented method is related to its simplicity in the handling of FSI coupling, that allows both fluid and solid particles to follow the same ISPH numerical scheme. As a result, no interface between solid and fluid domains is required, avoiding a well-known challenge in partitioned FSI schemes, where the fluid-solid interface must be handled to obtain sufficiently accurate matching solutions between the two domains. Modelling fluid and structure with a unified solver necessitates certain assumptions, such as uniform discretisation density for both domains, and a material density equal to that of the fluid, constant during the analysis; which implies incompressibility and a fixed Poisson's ratio of 0.5. While these assumptions may seem restrictive, they are generally accepted for cardiovascular soft tissues [87,88], and fixed Poisson's ratios are commonly employed in classical lattice spring models [76].

The proposed FSI approach is validated with a benchmark computational test and applied to model the dynamics of the aortic valve, which is a complex cardiovascular test case.

2. SPH basic idea and incompressible scheme

SPH is a Lagrangian mesh-less method where particles are used to represent the computational domain. Variables at each particle are obtained by means of discrete convolution integrals with filter functions, known as *kernel functions, W*. A very important feature of *kernel functions* is the characteristic length, known as *smoothing length, h*, which defines the influence domain of *W*. The generic *i* particle placed at the $\boldsymbol{x}_i$ position has a *support domain*, Ω_i, which contains all the surrounding *j* particles whose distance from $\boldsymbol{x}_i$ is lower than $k \cdot h$, where *k* is a specific constant of *W*. In this study, the Wendland function [89] was used (where $k = 2$). Particles are distributed based on the isotropic initial particle distance Δ_x, which is proportional to *h*. In this study Δ_x was set equal to $k \cdot h/2$, as recommended in the literature [83,90–92].

The generic function φ at the $\boldsymbol{x}_i$ position, φ_i, can be obtained through the function value at the neighbouring *j* particles (φ_j) laying in Ω_i, whose total number is N_i:

$$\varphi_i = \sum_{j=1}^{N_i} \frac{m_j}{\rho_j} \varphi_j W_{ij}; \tag{1}$$

where m_j and ρ_j are mass and density of *j* and $W_{ij} = W(\boldsymbol{x}_i - \boldsymbol{x}_j, h)$.

Two different techniques can be adopted to model fluid flows: weakly compressible (WCSPH) and truly incompressible (ISPH) approaches. In WCSPH, an equation of state is introduced to relate pressure and density; whilst ISPH uses a fractional-step procedure to solve the momentum and continuity equations. This work is based on the ISPH algorithm, where the pressure field is obtained implicitly by solving a system of *pressure Poisson equations* (PPEs), following the fractional-step technique of Chorin [93]. The employed fractional-step procedure, described in detailed in Monteleone et al. [92]. In brief, the momentum equation is firstly solved removing the pressure gradient term, to obtain the intermediate velocity $\boldsymbol{u}^*$ (predictor-step):

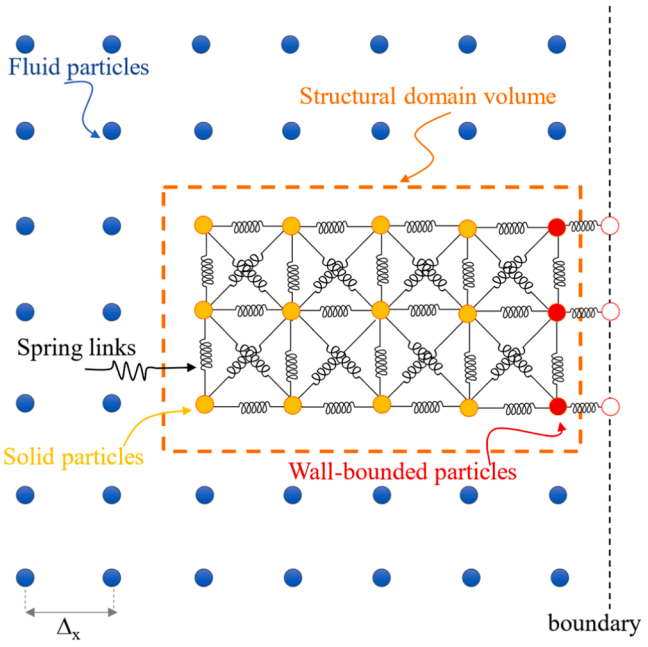

Fig. 1. 2D Sketch of the identification of the solid particles. Fluid particles: blue circles; structural domain: orange dashed line; solid particles: yellow circles; wall-bounded solid particles: red circles; ghost solid particles: empty red circles; boundary: dashed black line. (for interpretation of the references to colour in this figure legend, the reader is referred to the web version of this article).

$$\frac{\boldsymbol{u}_i^* - \boldsymbol{u}_i^{(r)}}{\Delta t} + \frac{3}{2}\boldsymbol{D}_i^{(r)} - \frac{1}{2}\boldsymbol{D}_i^{(r-1)} - \boldsymbol{f}_i = 0;$$

with

$$\boldsymbol{D}_i = -\sum_{j=1}^{N_i} m_j (\nu_i + \nu_j) \frac{(\boldsymbol{x}_i - \boldsymbol{x}_j)\cdot\nabla W_{ij}}{d_{ij}^2} (\boldsymbol{u}_i - \boldsymbol{u}_j); \tag{2}$$

where Δt is the time step, the index *r* indicates the time instant, $\boldsymbol{u}_i^*$ is the intermediate velocity of the *i* particle, $\boldsymbol{u}_i^r$ is the velocity at time *r*, $\boldsymbol{f}_i$ is the force per unit mass acting on the *i* particle, $\boldsymbol{D}_i$ is the diffusive term calculated using the Adams–Bashforth scheme [94], ∇W_{ij} is the gradient of *W*, ν_i and ν_j are the kinematic viscosities of particles *i* and *j*, and d_{ij} is the distance between *i* and *j*.

In order to correct the intermediate velocity, an irrotational corrective velocity field $\boldsymbol{u}^c$ is introduced, whose potential $\psi \cdot \Delta t$ is obtained by solving the PPEs system:

$$\sum_{j=1}^{N_i} \frac{2}{\rho_j} \frac{m_j (\boldsymbol{x}_i - \boldsymbol{x}_j)\cdot\nabla W_{ij}}{d_{ij}^2} (\psi_i - \psi_j) = \frac{1}{\Delta t} \sum_{j=1}^{N_i} \frac{m_j}{\rho_j} \left(\boldsymbol{u}_i^* - \boldsymbol{u}_j^*\right)\cdot\nabla W_{ij}; \tag{3}$$

where ψ is the pseudo-pressure.

In this work, the BiConjugate Gradient STABilized method (BiCGSTAB) proposed by Van der Vorst [95] was employed to solve the PPEs system using a preconditioning algorithm [96]. The BiCGSTAB is particularly suitable, due to the non-symmetricity and diagonal dominant of the coefficient matrix of the PPEs system [92].

The updated velocity $\boldsymbol{u}_i^{(r+1)}$ is therefore calculated in the corrector-step:

$$\boldsymbol{u}_i^{(r+1)} = \boldsymbol{u}_i^* + \boldsymbol{u}_i^c = \boldsymbol{u}_i^* - \Delta t \sum_{j=1}^{N_i} \frac{m_j}{\rho_j} (\psi_i - \psi_j) \nabla W_{ij}. \tag{4}$$

In this work, the use of mirror particles is employed to impose suitable boundary conditions and to overcome the truncation of the *kernel function* at the walls. This method involves an adequate covering of near boundary regions through the mirroring of the particles close to the

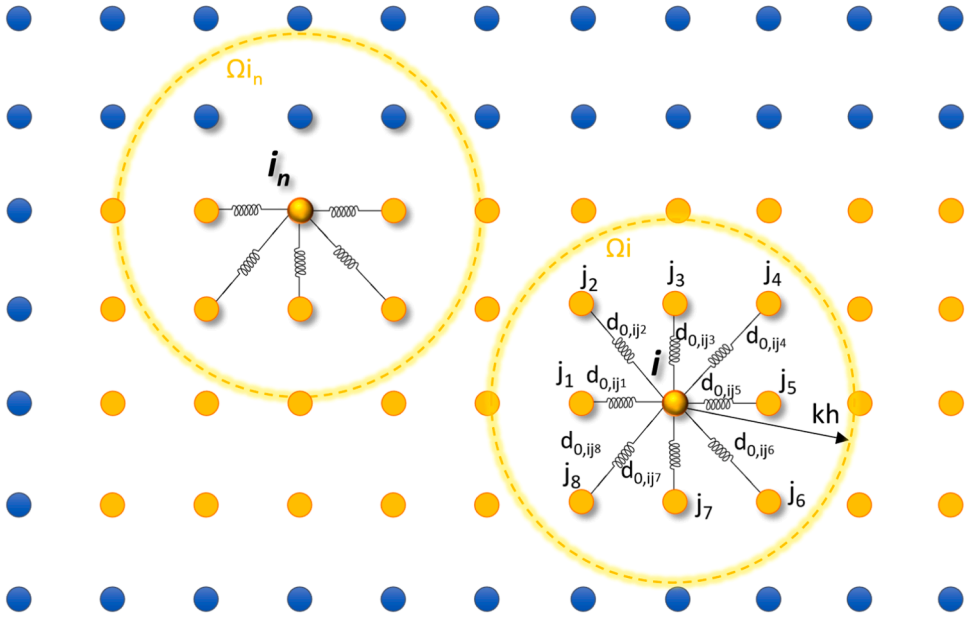

Fig. 2. 2D Sketch of the support domain (dashed lines) for two solid particles i and i_n with the springs associated to the neighbours solid particles.

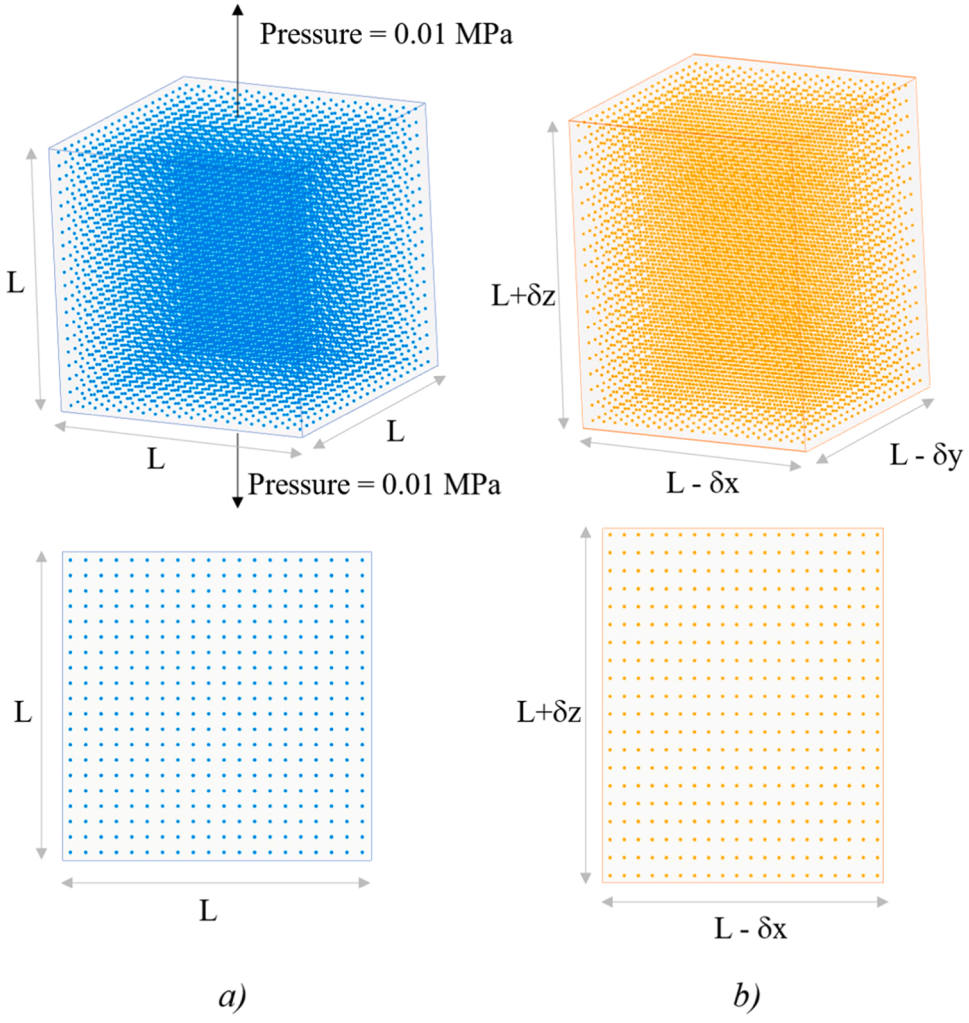

Fig. 3. Geometry and boundary condition for uniaxial tensile test used for the spring constant calibration. Perspective and front views on the top and bottom, respectively. a) Particles in the reference configuration; b) particles in the deformed configuration.

wall, enforcing the desired boundary conditions (adherence, free-slip, wall-law, Neumann, periodic, etc.), even for complex fluid domain geometries [83,90–92]. For a detailed description of the mirror particle procedure see Napoli et al. [83]. Moreover, the approach described in Monteleone et al. [92] is used for the inflow/outflow boundaries handling.

In order to overcome the tensile instability problem related to the particle clustering [97], the algorithm proposed by Xu et al. [98] is employed in this study. This procedure consists in shifting slightly the particles across streamlines, allowing to maintain an ordered particle distribution.

3. The proposed FSI method

3.1. Solid particles identification and treatment

As discussed in Section 2, fluid particles are initially arranged at a constant distance Δ_x in all cartesian directions. The fluid particles lying within the structural domain are geometrically identified and labelled as "solid" particles. Although the process is applied to a volumetric 3D system, in Fig. 1 it is schematised in 2D for simplicity of representation. The structural domain representative of a volume is drawn as a rectangle (dashed orange line). The particles within the structural domain are identified as solid particles (yellow circles), and springs ties are introduced between them. Further, solid particles close to the boundary (red circles) are also bounded to the wall, introducing a ghost solid particle in the direction normal to the wall (empty red circles).

At the start of the simulation, the list of the support domain used for the particle approximation is created per each particle (Eq. (1)) and then updated at each time step after the particles displacement. For each solid particle, an additional list of neighbour solid particles and resting distances is generated and kept unchanged during the simulation. This defines the solid domains and its unloaded configuration. In the example shown in Fig. 2, the support domain of the solid particle i encompasses $n = 8$ neighbour solid particles (j_1 to j_8) with initial resting distance $d_{0,i-j_n}$. These particles are linked to particle i with springs.

Springs that experience tension or compression respond by applying internal elastic forces in the attempt to restore their unloaded length. The total internal force per unit mass acting on the generic solid particle i, $\boldsymbol{f}_i$, can be expressed as:

$$\boldsymbol{f}_i = \frac{k_e\,\Delta_x}{m_i}\sum_{j=1}^{N}\left(d_{0,ij} - d_{ij}\right)\hat{\boldsymbol{x}}_{ij}; \tag{5}$$

where the summation is extended to the total number N of solid (effective and ghost) particles connected to i (eight particles in Fig. 2), k_e is the spring constant normalised over the initial distance (Δ_x), and $\hat{\boldsymbol{x}}_{ij} = (\boldsymbol{x}_i - \boldsymbol{x}_j)/d_{ij}$ is the unit vector directed from i to j.

This force is added in the momentum equations as a mass force. Considering the fractional-step scheme used in this work, $\boldsymbol{f}_i$ is included in the predictor-step (Eq. (2)).

It is important to note that the FSI coupling is achieved inherently within the modelling framework, as both fluid and solid particles are solved simultaneously within a unified ISPH numerical scheme, without the need to explicitly define interfaces.

3.2. Elastic constant calibration

Springs connecting solid particles have a normalised elastic constant k_e, whose value controls the stiffness of the structure. The calibration of the law associating k_e with the Young's modulus of the homogenised material was carried out by simulating uniaxial tensile tests on a solid cube, as described in Monteleone et al. [82] and Monteleone et al. [99]. The cube, of side 0.1 m, consisted of 8000 solid particles, with $k \cdot h$ equal to 0.01 m. The solid block was stretched by imposing a pressure load equal to 0.01 MPa on the top and bottom surfaces (see Fig. 3), and zero pressure on the other faces.

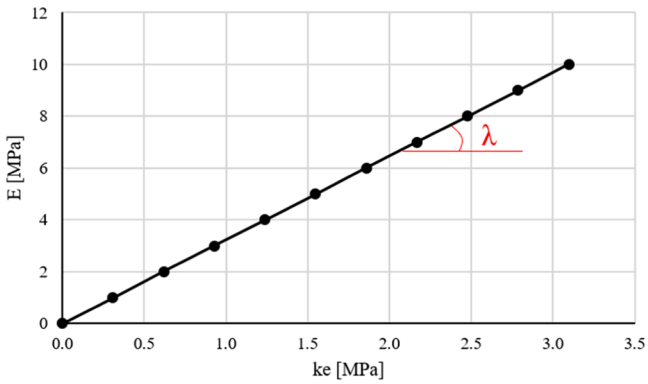

Fig. 4. Relationship obtained from the spring constant calibration, where $E = \lambda \cdot k_e$ and $\lambda = 3.23$.

A set of simulations was performed, measuring the Young's modulus E and the Poisson's ratio ν_s for a range of normalised spring constants k_e ranging from 0 to 3.1 MPa. A basic linear law was identified (in Fig. 4), where $E = \lambda \cdot k_e$; with $\lambda = 3.23$. It was verified that, coherently with the material incompressibility condition commonly accepted for soft tissue constitutive models [87,88], ν_s remains constant and equal to 0.5. In order to verify the influence of the starting particle distance, the analysis was repeated with $k \cdot h = 0.005$ m. Results confirmed that the variation in $k \cdot h$ did not produce any change in the relation identified between E and k_e.

3.3. Flow-chart of the proposed method

The sequence of actions of the proposed FSI algorithm is reported below:

- ACTION 1 – *Identify solid and wall-bound particles*. The solid particles are geometrically identified based on the solid domain boundaries. Moreover, the solid particles having a distance less than Δ_x are linked to the wall introducing ghost solid particles;
- ACTION 2 – *Create solid particles neighbour list*. For each solid particle, the list of the neighbour solid particles at a distance inferior to $k \cdot h$ is created and recorded for the whole simulation;
- ACTION 3 – *Create support domain and mirror*. The support domain of each particle is created including all the surrounding particles (fluid and solid) with distance lower than $k \cdot h$. Moreover, to overcome the truncation of the support domain at the boundaries, the mirror particles procedure is used. Specifically, the particles having distance from the boundaries shorter than $k \cdot h$ generate mirror particles along the directions normal to the boundary. Mirror particles have the same physical properties of the generating particles, while the velocity is imposed to ensure that boundary conditions are satisfied;
- ACTION 4 – *Calculate internal solid forces*. For each solid particle, the total force resulting from the system of neighbouring springs (effective and ghost) is calculated through Eq. (5).
- ACTION 5 – *Predictor-step*. The intermediate velocity $\boldsymbol{u}^*$ is calculated through Eq. (2), including for the solid particles the force calculated at ACTION 4;
- ACTION 6 – *PPE system*. The pseudo-pressure ψ is calculated solving the system made of one PPE (Eq. (3)) per each particle;
- ACTION 7 – *Corrector-step*. Eq. (4) is used to correct $\boldsymbol{u}^*$, obtaining the updated velocities $\boldsymbol{u}^{r+1}$;
- ACTION 8 – *Update particle position*. Particles are moved in the updated position $\boldsymbol{x}^{r+1}$ using the mean value of the new and old velocities ($\boldsymbol{u}_i^{r+1}$ and $\boldsymbol{u}_i^r$, respectively);

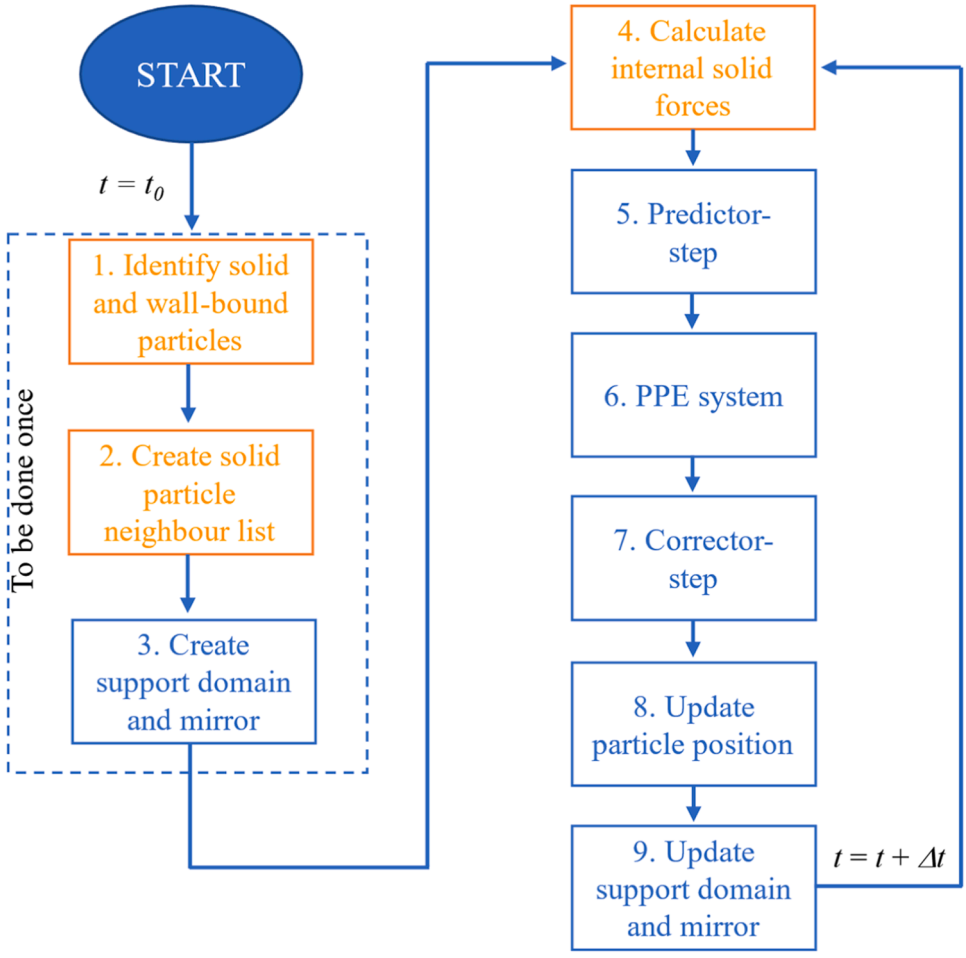

Fig. 5. Flow-chart of the proposed FSI algorithm. Actions specifically for the solid particles treatment are highlighted in orange. The actions inside the dashed rectangle are performed only once at the beginning of the simulation. (For interpretation of the references to colour in this figure legend, the reader is referred to the web version of this article).

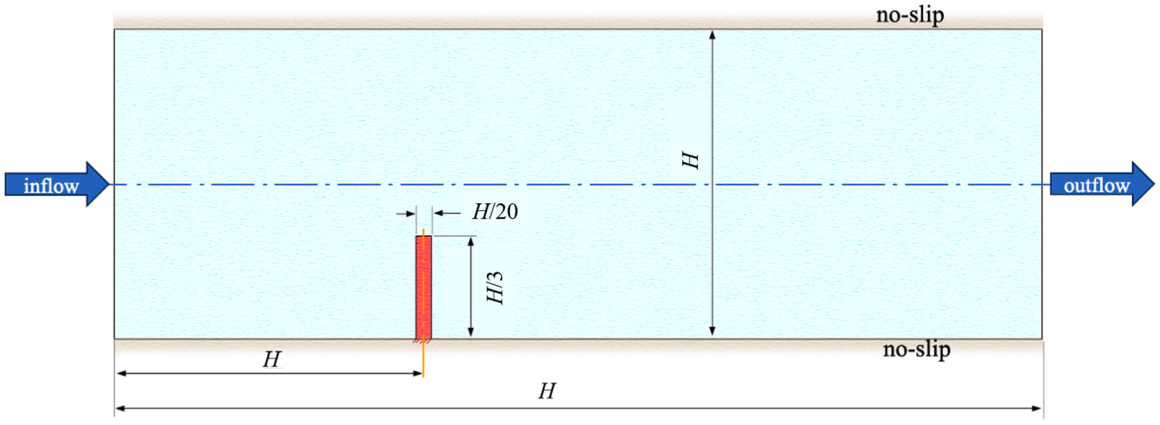

Fig. 6. Benchmark test case – Channel and beam dimensions and boundary conditions. $H = 0.3$ m.

- ACTION 9 – *Update support domain and mirror*. After calculating the updated particle position, the particle support domain and the mirror particles are updated (see ACTION 3).

After ACTION 9, the simulation time is advanced by one time step ($t = t + \Delta t$), and the procedure is reiterated from ACTION 4. Fig. 5 shows a flow-chart of the proposed FSI algorithm.

4. Results and discussion

4.1. Benchmark test case - Elastic beam immersed in a channel flow

An elastic beam immersed in a channel was used as a benchmark case to validate the code. Fig. 6 shows the channel and beam dimensions and the boundary conditions. The channel was designed with height $H = 0.3$ m and length $3H$. An elastic beam of height $H/3$ and width $H/20$ was

Table 1
Benchmark test case – parameters of the simulation.

Parameter	Value
Channel height (H)	0.3 m
Fluid density (ρ_f)	1000 kg/m^3
Dynamic viscosity (μ)	1 Pa s
Inlet mean velocity ($\overline{u}$)	0.5 m/s
Reynolds number (Re)	150
Structure density (ρ_s)	1000 kg/m^3
Young's modulus (E)	0.7 MPa
Poisson's ratio* (ν_s)	0.4999

* used for ANSYS simulation.

positioned at a distance H from the channel inflow section. The beam was fully constrained at the channel bottom surface.

Adherence boundary condition was imposed on the top and bottom walls of the channel, while inflow and outflow boundary conditions were employed at the left and right sides of the fluid domain, respectively. Specifically, zero pressure was imposed at the outflow section, while a parabolic velocity was prescribed at the inlet as follows:

$$u(x,t) = \begin{cases} 1.5\,\overline{u}\,\dfrac{y\,(H-y)}{(H/2)^2}\,\dfrac{t}{t^*} \;\; for\; t < t^* \\ 1.5\,\overline{u}\,\dfrac{y\,(H-y)}{(H/2)^2} \;\; for\; t > t^* \end{cases} \tag{6}$$

where t is the time, $\overline{u}$ was set equal to 0.5 m/s and $t^* = 1$. Hence, the inlet mean velocity increases linearly from zero to 0.5 m/s in the first second (from 0to t^*), and then stabilises to the value of 0.5 m/s.

Fluid and solid densities are imposed both equal to $\rho_f = \rho_s = 1000$ kg/m^3 and the fluid dynamic viscosity is imposed equal to $\mu = 1$ Pa·s. The resulting Reynolds' number is $Re = \overline{u}\,H\,\rho_f/\mu = 150$. The Young's modulus of the beam material was set equal to 0.7 MPa. The parameters of the simulation are summarised in Table 1.

The commercial software *ANSYS* (Ansys® Academic Research Mechanical, Release 2022 R2) was used for comparison. Specifically, the structural domain was analysed using the *ANSYS Transient Structural* module, whilst the fluid dynamics simulation was performed with the *ANSYS CFX* package. For the structural domain, due to the inability of finite element methods to handle incompressible materials, a Poisson's ratio ν_s= 0.4999 was imposed. The structural and fluid solutions were coupled by means of the *System Coupling* available in Ansys workbench, which handles the data transfer between individual physics solvers [100].

A smoothing length of 3.75 × 10^{-3} m was selected for the SPH domain, resulting into 19,200 particles. A linear structured mesh with identical element size (3.75 × 10^{-3} m) was used for the ANSYS discretisation.

In the SPH simulation, the particles lying within the beam region were defined as solid, linking the beam particles in contact with the lower wall of the channel by introducing ghost solid particles, as discussed in Section 3.1.

Fig. 7 shows the velocity field at time instant t =1 s, obtained with the proposed FSI algorithm and with the *ANSYS System Coupling* approach. As it can be observed, results appear in very good agreement.

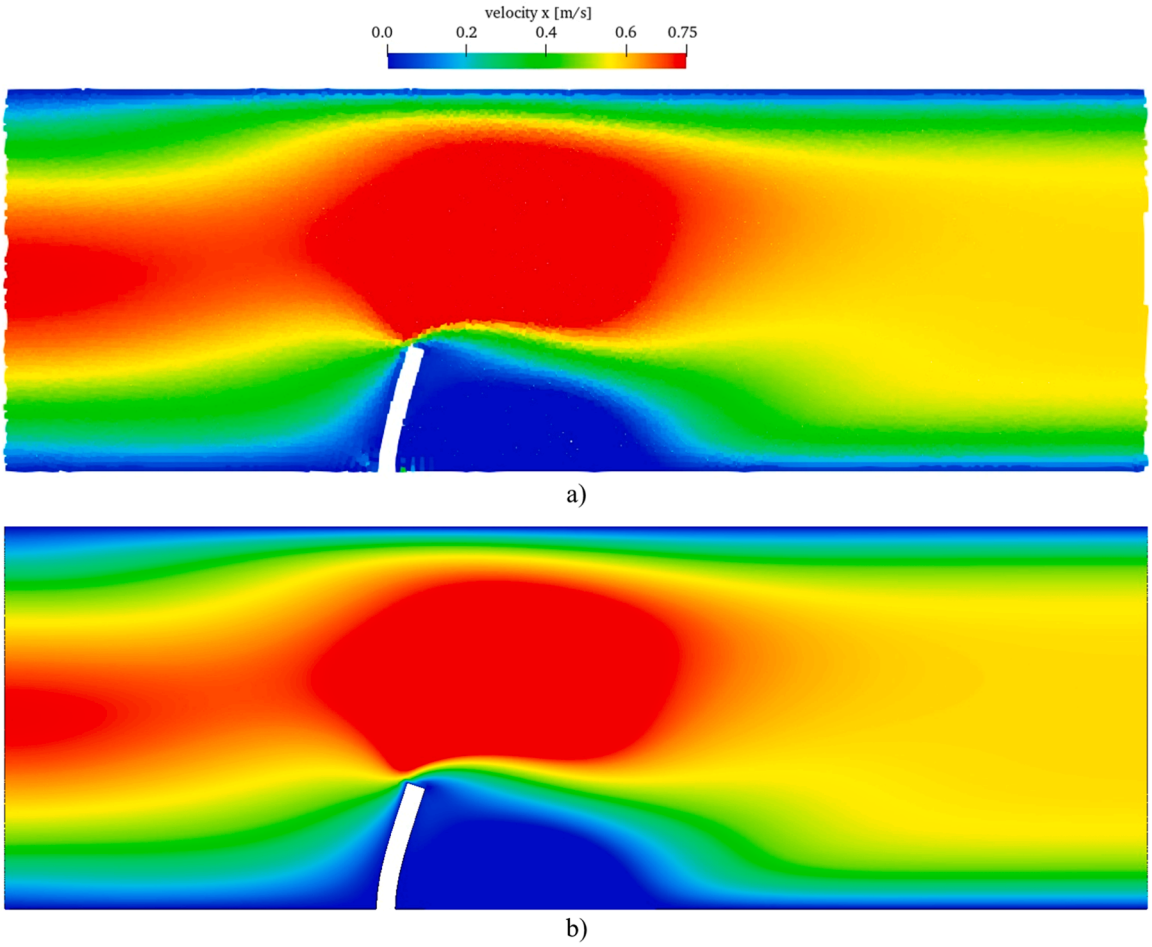

Fig. 7. Benchmark test case – Streamwise velocity at t = 1 s: a) SPH; b) ANSYS. (For interpretation of the references to color in this figure legend, the reader is referred to the web version of this article.)

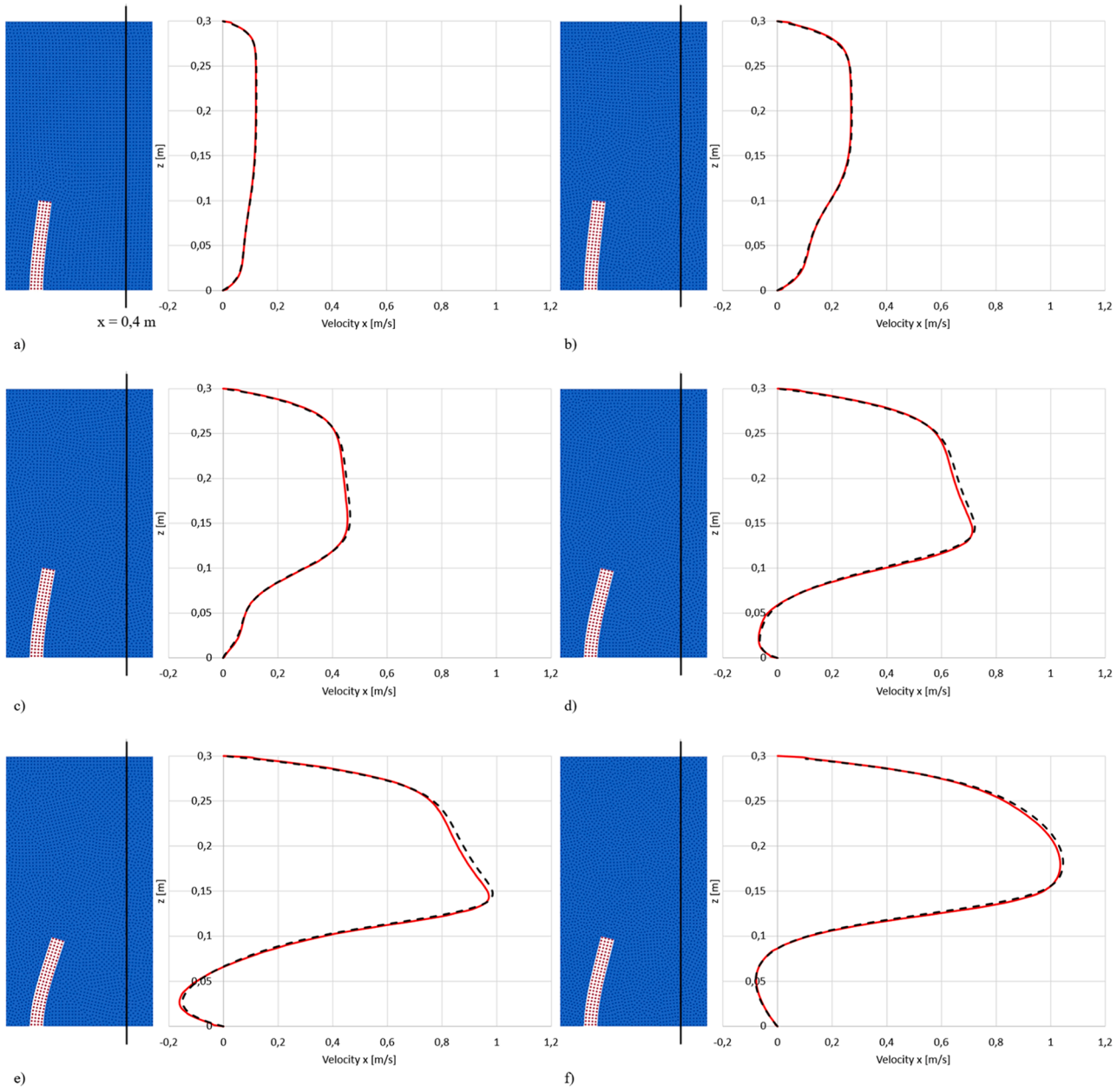

Fig. 8. Benchmark test case – Comparison of beam position on the left: ANSYS fluid domain (blue region) and SPH solid domain (red particles); velocity profiles at $x = 0.4$ m on the right: ANSYS (dashed black line) and SPH (continuous red line). Considered time instants: a) $t = 0.2$ s; b) $t = 0.4$ s; c) $t = 0.6$ s; d) $t = 0.8$ s; e) $t = 1$ s; f) $t = 3$ s. (For interpretation of the references to colour in this figure legend, the reader is referred to the web version of this article.)

In order to provide a quantitative comparison, the beam deformation is compared for the two solvers at six different time instants, as shown in Fig. 8. For clarity of representation, the ANSYS fluid domain (blue region) is superposed with the SPH solid domain (red particles). The velocity profiles computed downstream of the beam, at position $x = 0.4$ m (indicated with a black line in the figure) are reported. Differences in the velocities at each location are less than 3 %, confirming the accuracy of the proposed FSI algorithm.

A comparison of the computational costs was also performed, running the simulation on an AMD EPYC 7402 – 2.8 GHz processor with 2 sockets and 24 cores per sockets. Considering one CPU, the proposed FSI approach results 6.5 times more efficient than the method used for comparison. Still, thanks to its simplicity, the proposed FSI algorithm is fully integrated in the parallel computing scheme of Monteleone et al. [101], allowing further improvement of efficiency by increasing the number of CPUs.

4.2. Aortic valve simulation

The simulation of the heart valves function remains one of the most challenging FSI case studies in cardiovascular engineering, where the limits of the different FSI approaches commonly become evident. In particular, the aortic valve is one of the most relevant clinical components, as this valve is subjected to the severe operating conditions experienced in the left heart and is more prone to be affected by congenital or acquired diseases [102]. The aortic valve is a trileaflet valve located between the left ventricle and the aorta, which regulates the unidirectionality of the oxygenated blood flow ejected from the left ventricle to feed the body tissues. In particular, during systole (ventricular contraction) the valve is opened by the ejected flow and its leaflets should hamper the flow as little as possible. During diastole, when the ventricular muscle relaxes, the valve leaflets are driven into contact by the flow returning from the aorta to the left ventricle,

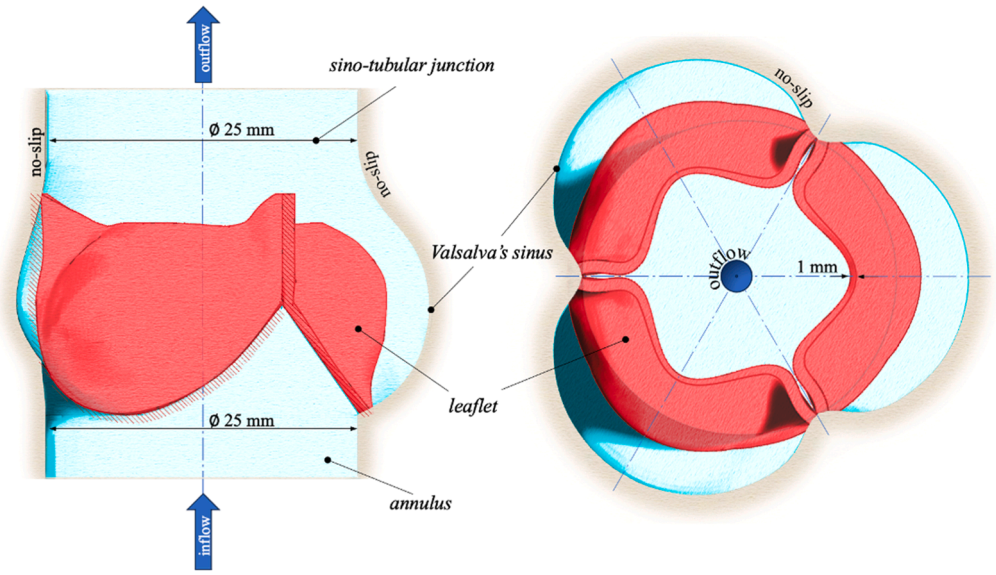

Fig. 9. Aortic valve simulation – Geometry of the Valsalva sinuses and leaflets. Sagittal and transversal views.

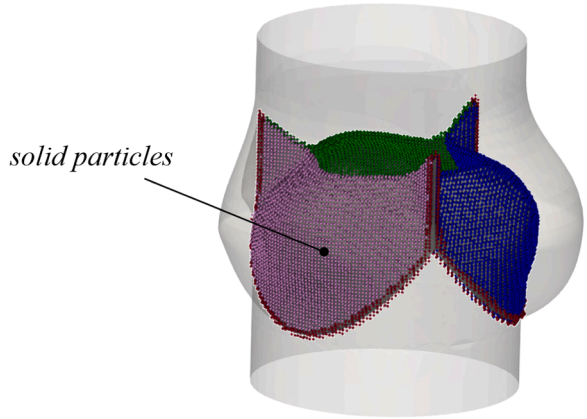

Fig. 10. Aortic valve simulation – Solid particles defining the valve leaflets: blue, green and magenta circles; red circles: constrained solid particles at the commissures. (For interpretation of the references to colour in this figure legend, the reader is referred to the web version of this article.).

resulting in the valve closure and arresting the backflow. During normal functioning, the valve is subjected to large transvalvular pressure differences up to about 120 mmHg.

The modelling of such problem is very challenging due to the large deformations experienced by the structural components (the leaflets) as effect of their interaction with a pulsatile blood flow, and the periodical contact between the valve leaflets during coaptation [5].

In the test case presented, geometries of the aortic root and the valve are taken from Tango et al. [103]. In particular, the aortic annulus and sino-tubular junction (region where the aortic root returns circular after bulging out at the level of the leaflets) have identical diameter, equal to 25 mm. The leaflets geometry is based on the description of the idealised healthy human aortic valve proposed by Thubrikar [104] and pre-expanded to a semi-opened reference configuration. The Valsalva sinuses, that are the three pouches at the base of the aortic root facing each of the valve leaflets (see Fig. 9), are assumed identical in shape and size. Their maximum cross section is defined by an epitrochoid circumscribed to a circle of diameter equal to 25 mm and inscribed into a circle of diameter equal to 36.44 mm. The root inner volume (blood and leaflets) was discretised with a smoothing length of 0.325 mm, resulting in a total number of 583,000 particles. The leaflets were modelled with a thickness of 1 mm, comprising three layers of particles.

Fig. 10 shows the computational domain of the root and the valve. Leaflets are modelled as separate solids (represented in magenta, blue and green), in order to allow the valve whole opening. Moreover, solid particles close to the aortic wall (indicated in red) are constrained by introducing ghost particles, as discussed in Section 3.1.

Blood was treated as an incompressible Newtonian fluid, which is a common assumption [24,27,33,103,105–107], with dynamic viscosity of 0.0035 Pa·s and density of 1060 kg/m^3.

The material properties of the native aortic leaflets are reported to be non-linear, incompressible and anisotropic [108–111]. This behaviour is the result of the biomechanical synergy between elastin and collagen fibres, and supports the valve function by optimising the leaflets mechanical response during the cardiac cycle. In fact, during valve opening, when the level of membrane strain is reduced, collagen fibres maintain a coiled configuration, which confers to the material high flexibility [112]. When the valve closes and leaflets coapt to retain the returning blood flow, fibres are uncoiled by the increasing transmural pressure, resulting in substantially higher tissue rigidity. This non-linear behaviour is neglected in the present study, where leaflets are modelled as linear elastic. Hence, in order to account for the described change in response of the material in the different phases of the valve cycle, different Young's moduli are set for the valve opening and closing stages, equal to 20 kPa and 200 kPa, respectively. These values allow to obtain similar flexural rigidities as reported in the literature for the healthy aortic leaflets [31,113–115].

The aortic root walls are modelled as rigid with no-slip boundary conditions (aortic compliance is neglected). A pressure corresponding to the physiological transvalvular pressure difference is applied at the ventricular side of the domain, while pressure at the aortic outlet is kept equal to zero. Specifically, a maximum of 8 mmHg was imposed with a

Table 2
Aortic valve simulation – parameters.

Parameter	Value
Fluid density (ρ_f)	1060 kg/m^3
Dynamic viscosity (μ)	0.0035 Pa s
Inlet maximum pressure during opening	8 mmHg
Inlet maximum pressure during closing	120 mmHg
Structure density (ρ_s)	1060 kg/m^3
Young's modulus of leaflets during opening (E_o)	0.02 MPa
Young's modulus of leaflets during closing (E_c)	0.20 MPa

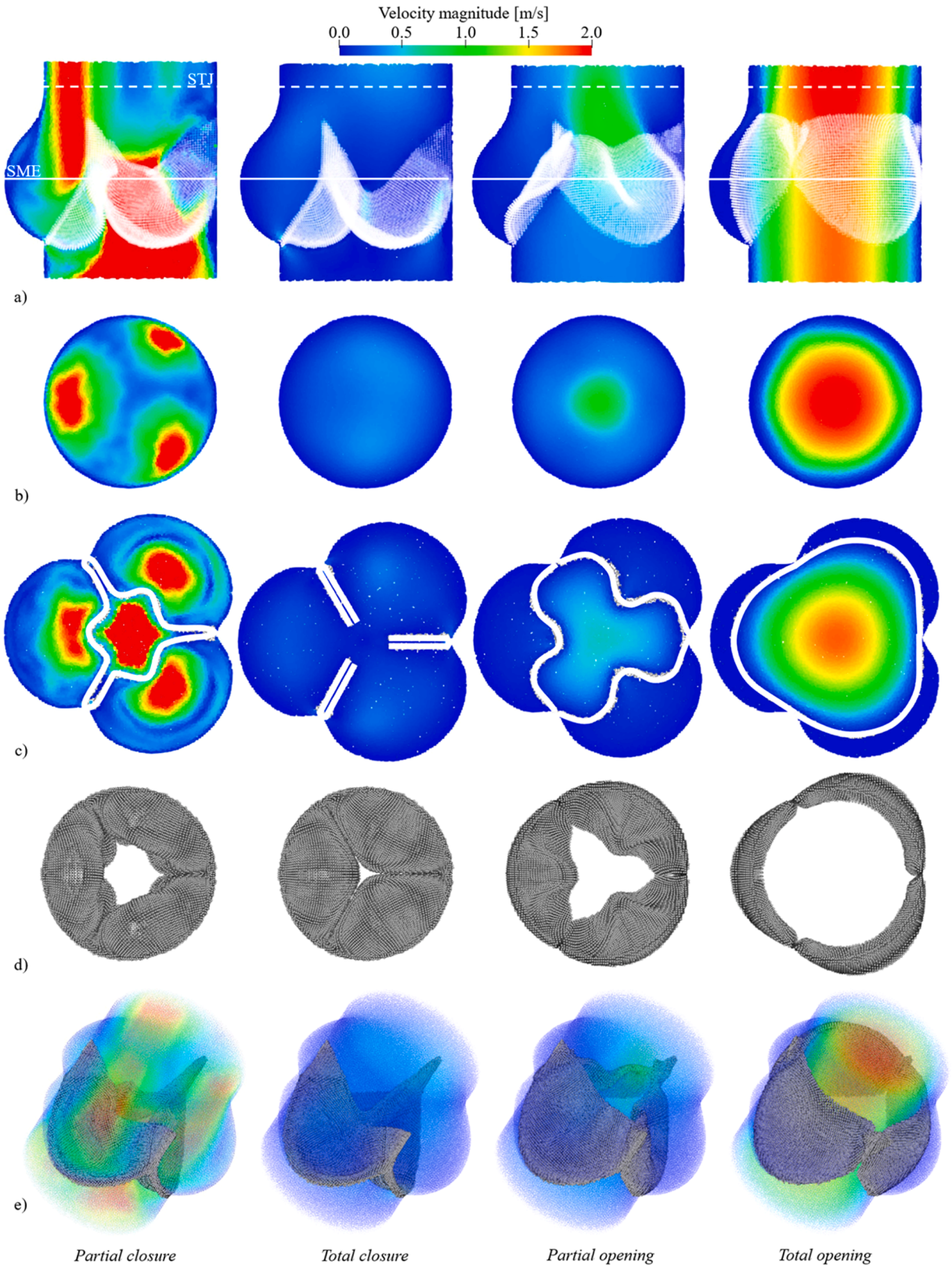

Fig. 11. Aortic valve simulation – Velocity field and leaflet position at four time instants. a) Sagittal section; b) transversal cross section at the sino-tubular junction (STJ) indicated as dashed white line; c) transversal cross section at the Valsalva sinuses maximum expansion (SME) indicated as continuous white line; d) leaflets position; e) perspective view. (For interpretation of the references to color in this figure legend, the reader is referred to the web version of this article.)

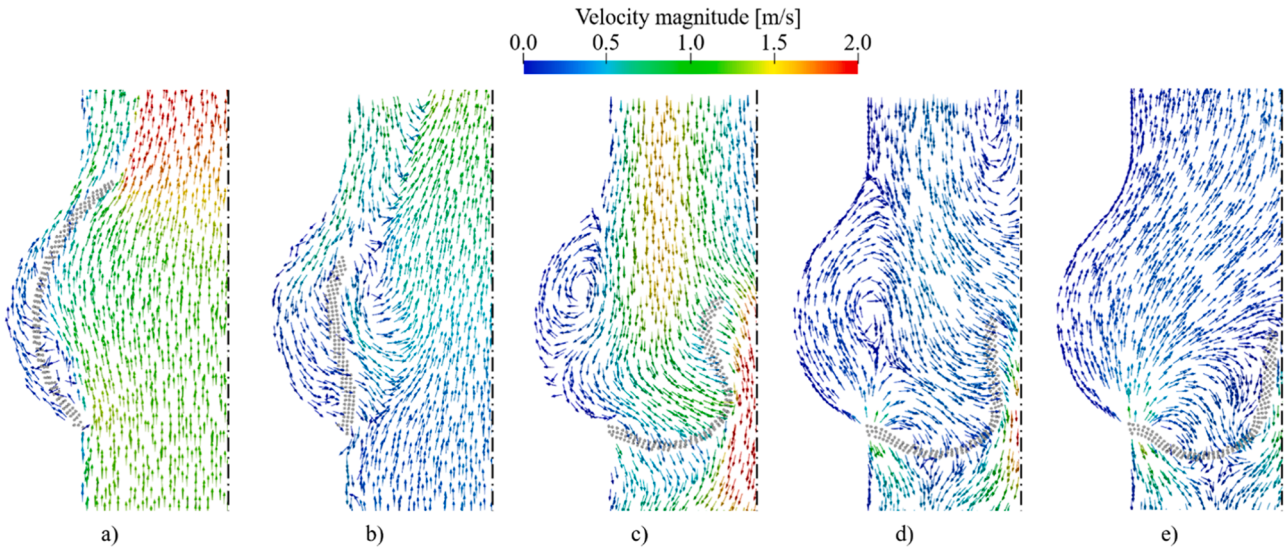

Fig. 12. Aortic valve simulation – Velocity vectors at different instants of the closing phase. a) Full open valve configuration; b, c and d) partial closure; e) full closure. All vectors are represented with identical length, and their magnitude is indicated by their colour, as described in the colour bar on top of the figure. (For interpretation of the references to colour in this figure legend, the reader is referred to the web version of this article.)

linear ramp during valve opening; then the gradient inverts during closing, imposing a maximum transvalvular pressure difference of 120 mmHg. Parameters used in the simulation are reported in Table 2.

Fig. 11 shows the results at four different time instants corresponding to: partial and full closing, partial and full opening. The velocity field at the sagittal plane is reported in Fig. 11a, while the cross-sections at the sino-tubular junction (STJ) and at the sinuses maximum expansion (SME) are shown in Fig. 11b and c, respectively. Moreover, the valve configuration is displayed in Fig. 11d.

Leaflets configurations appear to realistically reproduce the opening and closing of the aortic valve. In fact, in the closing phase, leaflets approach each other until complete coaption at the diastolic phase. Then, during the opening phase, leaflets move apart allowing a central jet. A perspective view is provided in Fig. 11e. Although only a qualitative comparison can be made due to the simplifications in the material properties, results are coherent to those reported in Tango et al. [103]. In fact, leaflets expand widely into the Valsalva sinuses when open, minimising their interference with the ejecting flow (Fig. 12a). This effect allows to maximise the valve geometric orifice area and, as a consequence, the effective orifice area, which is a parameter descriptive of the systolic valve performance [116].

This result appears to be coherent also with the experimental study from Di Leonardo et al. [117], where leaflets of an *ex vivo* porcine aortic root show the same opening mechanism. In the closing phase, the back flow that forms along the aortic wall drives the leaflets from their fully open configuration towards the centre (Fig. 12b), and then separates producing a vortex into the Valsalva sinuses (Fig. 12c). This progressively expands and moves the leaflets centripetally (Fig. 12d), until complete closure is achieved (Fig. 12e). These washout vortices, already described by Tango et al. [103], are believed to form and propagate to prevent blood stagnation.

The analysis confirms that the proposed SPH method is able to capture complex cardiovascular problems such as the aortic valve dynamics, avoiding the main limitations of current competing approaches. In fact, thanks to the mesh-less nature of the SPH method, no issues associated with the remeshing procedure, which characterise ALE approaches, are present. On the other hand, contrary to IB methods, the unique solution obtained by solving a single system requires no additional coupling procedures nor interpolation at the interface. Furthermore, contact between coapting structures (e.g. in valve closing simulations) is intrinsically permitted, requiring no artefactual gaps or complex contact algorithms. This implies additional saving in computational time to what already discussed in Section 4.1. Furthermore, the proposed FSI algorithm is suitable to incorporate non-Newtonian and thrombogenic models, such as that recently proposed by Monteleone et al. [99], to investigate the thrombogenicity associated with different operating conditions or devices.

A limitation of the method is the basic description of the material constitutive laws, which neglects non-linearity, viscoelasticity and anisotropy. This is common to current FSI solvers based on particle methods, although continuous advances are being made to improve the material description [35,118]. The implementation of non-linear responses based on strain energy, viscoelastic and anisotropic behaviours will be the next steps of development. Also, the particle density must be sufficient to model thin wall structures, such as the valve leaflets (although the possibility to use multi-domain approaches with variable smoothing lengths [91] may address this issue).

Finally, the method may not be accurate when modelling phenomena involving structure and fluid with very different densities, subjected to highly dynamic motion.

5. Conclusions

A novel FSI technique is proposed using the Lagrangian mesh-less SPH method. In this approach, both fluid and structural domains are represented by particles. In order to model the structural behaviour, spring bounds are introduced between neighbouring solid particles and elastic forces are determined aiming at restoring the springs resting length. The calculated forces are introduced in the fractional-step procedure used in the ISPH scheme.

Despite the simplicity in the structural modelling, the proposed approach shows good accuracy when compared with benchmark test cases typically used to validate FSI models. Moreover, the method was successfully applied to model a complex cardiovascular problem, consisting in the analysis of the aortic valve dynamics.

The approach has shown the ability to overcome the typical issues related to this type of simulations, obtaining results in agreement with the literature. Since the approach is integrated in a truly incompressible method, it is particularly suitable to model soft tissues which exhibit an incompressible behaviour. However, material properties of the soft tissues are still simplified and incorporating non-linear behaviours, based on strain energy, and anisotropy will be the next step of development.

CRediT authorship contribution statement

Alessandra Monteleone: Conceptualization, Data curation, Formal analysis, Investigation, Methodology, Software, Validation, Writing – original draft, Writing – review & editing. **Sofia Di Leonardo:** Conceptualization, Data curation, Formal analysis, Validation, Writing – original draft, Writing – review & editing. **Enrico Napoli:** Conceptualization, Methodology, Software, Supervision, Writing – review & editing. **Gaetano Burriesci:** Conceptualization, Data curation, Investigation, Methodology, Project administration, Supervision, Validation, Writing – original draft, Writing – review & editing.

Declaration of competing interest

The authors declare that they have no known competing financial interests or personal relationships that could have appeared to influence the work reported in this paper.

References

[1] E.H. Dowell, K.C. Hall, Modeling of fluid-structure interaction, Annu Rev. Fluid. Mech. 33 (2001) 445–490, https://doi.org/10.1146/annurev.fluid.33.1.445.

[2] G. Hou, J. Wang, A. Layton, Numerical methods for fluid-structure interaction — a review, Commun. Comput. Phys. 12 (2012) 337–377, https://doi.org/10.4208/cicp.291210.290411s.

[3] T.B. Le, M. Usta, C. Aidun, A. Yoganathan, F. Sotiropoulos, Computational methods for fluid-structure interaction simulation of heart valves in patient-specific left heart anatomies, Fluids 7 (2022) 94, https://doi.org/10.3390/fluids7030094.

[4] M. Hirschhorn, V. Tchantchaleishvili, R. Stevens, J. Rossano, A. Throckmorton, Fluid–structure interaction modeling in cardiovascular medicine – A systematic review 2017–2019, Med. Eng. Phys. 78 (2020) 1–13, https://doi.org/10.1016/j.medengphy.2020.01.008.

[5] T. Terahara, K. Takizawa, T.E. Tezduyar, Y. Bazilevs, M.-C. Hsu, Heart valve isogeometric sequentially-coupled FSI analysis with the space–time topology change method, Comput. Mech. 65 (2020) 1167–1187, https://doi.org/10.1007/s00466-019-01813-0.

[6] J. Hron, M. Mádlík, Fluid-structure interaction with applications in biomechanics, Nonlinear. Anal. Real. World Appl. 8 (2007) 1431–1458, https://doi.org/10.1016/j.nonrwa.2006.05.007.

[7] F. Sturla, E. Votta, M. Stevanella, C.A. Conti, A. Redaelli, Impact of modeling fluid–structure interaction in the computational analysis of aortic root biomechanics, Med. Eng. Phys. 35 (2013) 1721–1730, https://doi.org/10.1016/j.medengphy.2013.07.015.

[8] G. Marom, Numerical methods for fluid–structure interaction models of aortic valves, Arch. Comput. Method. Eng. 22 (2015) 595–620, https://doi.org/10.1007/s11831-014-9133-9.

[9] M. Malvè, A. García, J. Ohayon, M.A. Martínez, Unsteady blood flow and mass transfer of a human left coronary artery bifurcation: FSI vs. CFD, Int. Commun. Heat Mass Transf. 39 (2012) 745–751, https://doi.org/10.1016/j.icheatmasstransfer.2012.04.009.

[10] S.T. Ha, L.C. Ngo, M. Saeed, B.J. Jeon, H. Choi, A comparative study between partitioned and monolithic methods for the problems with 3D fluid-structure interaction of blood vessels, J. Mech. Sci. Technol. 31 (2017) 281–287, https://doi.org/10.1007/s12206-016-1230-2.

[11] C. Michler, E.H. van Brummelen, S.J. Hulshoff, R. de Borst, The relevance of conservation for stability and accuracy of numerical methods for fluid–structure interaction, Comput. Methods Appl. Mech. Eng. 192 (2003) 4195–4215, https://doi.org/10.1016/S0045-7825(03)00392-X.

[12] M. Heil, A.L. Hazel, J. Boyle, Solvers for large-displacement fluid–structure interaction problems: segregated versus monolithic approaches, Comput. Mech. 43 (2008) 91–101, https://doi.org/10.1007/s00466-008-0270-6.

[13] J. Degroote, K.-J. Bathe, J. Vierendeels, Performance of a new partitioned procedure versus a monolithic procedure in fluid–structure interaction, Comput. Struct. 87 (2009) 793–801, https://doi.org/10.1016/j.compstruc.2008.11.013.

[14] M. Bucelli, L. Dede, A.Q. Null, C. Vergara, Partitioned and monolithic algorithms for the numerical solution of cardiac fluid-structure interaction, Commun. Comput. Phys. 32 (2022) 1217–1256, https://doi.org/10.4208/cicp.OA-2021-0243.

[15] J. Donea, S. Giuliani, J.P. Halleux, An arbitrary lagrangian-eulerian finite element method for transient dynamic fluid-structure interactions, Comput. Method. Appl. Mech. Eng. 33 (1982) 689–723, https://doi.org/10.1016/0045-7825(82)90128-1.

[16] M. Souli, A. Ouahsine, L. Lewin, ALE formulation for fluid–structure interaction problems, Comput. Method. Appl. Mech. Eng. 190 (2000) 659–675, https://doi.org/10.1016/S0045-7825(99)00432-6.

[17] E. Kuhl, S. Hulshoff, R. de Borst, An arbitrary Lagrangian Eulerian finite-element approach for fluid-structure interaction phenomena, Int. J. Numer. Method. Eng. 57 (2003) 117–142, https://doi.org/10.1002/nme.749.

[18] G. Lipari, E. Napoli, The impacts of the ALE and hydrostatic-pressure approaches on the energy budget of unsteady free-surface flows, Comput. Fluid. 37 (2008) 656–673, https://doi.org/10.1016/j.compfluid.2007.10.005.

[19] C.S. Peskin, Flow patterns around heart valves: a numerical method, J. Comput. Phys. 10 (1972) 252–271, https://doi.org/10.1016/0021-9991(72)90065-4.

[20] C.S. Peskin, D.M. McQueen, A three-dimensional computational method for blood flow in the heart I. Immersed elastic fibers in a viscous incompressible fluid, J. Comput. Phys. 81 (1989) 372–405, https://doi.org/10.1016/0021-9991(89)90213-1.

[21] C.S. Peskin, The immersed boundary method, Acta Numerica 11 (2002) 479–517, https://doi.org/10.1017/S0962492902000077.

[22] I. Borazjani, Fluid–structure interaction, immersed boundary-finite element method simulations of bio-prosthetic heart valves, Comput. Method. Appl. Mech. Eng. 257 (2013) 103–116, https://doi.org/10.1016/j.cma.2013.01.010.

[23] B.E. Griffith, N.A. Patankar, Immersed methods for fluid–structure interaction, Annu. Rev. Fluid. Mech. 52 (2020) 421–448, https://doi.org/10.1146/annurev-fluid-010719-060228.

[24] L. Ge, F. Sotiropoulos, A numerical method for solving the 3D unsteady incompressible Navier–Stokes equations in curvilinear domains with complex immersed boundaries, J. Comput. Phys. 225 (2007) 1782–1809, https://doi.org/10.1016/j.jcp.2007.02.017.

[25] N. Diniz dos Santos, J.-F. Gerbeau, J.-F. Bourgat, A partitioned fluid–structure algorithm for elastic thin valves with contact, Comput. Method. Appl. Mech. Eng. 197 (2008) 1750–1761, https://doi.org/10.1016/j.cma.2007.03.019.

[26] C.J. Carmody, G. Burriesci, I.C. Howard, E.A. Patterson, An approach to the simulation of fluid–structure interaction in the aortic valve, J. Biomech. 39 (2006) 158–169, https://doi.org/10.1016/j.jbiomech.2004.10.038.

[27] W. Mao, A. Caballero, R. McKay, C. Primiano, W. Sun, Fully-coupled fluid-structure interaction simulation of the aortic and mitral valves in a realistic 3D left ventricle model, PLoS One 12 (2017) e0184729, https://doi.org/10.1371/journal.pone.0184729.

[28] A.M. Bavo, G. Rocatello, F. Iannaccone, J. Degroote, J. Vierendeels, P. Segers, Fluid-Structure Interaction Simulation of Prosthetic Aortic Valves: comparison between Immersed Boundary and Arbitrary Lagrangian-Eulerian Techniques for the Mesh Representation, PLoS One 11 (2016) e0154517, https://doi.org/10.1371/journal.pone.0154517.

[29] T.E. Tezduyar, S. Sathe, Modelling of fluid–structure interactions with the space–time finite elements: solution techniques, Int. J. Numer. Methods Fluids. 54 (2007) 855–900, https://doi.org/10.1002/fld.1430.

[30] J. Sigüenza, D. Pott, S. Mendez, S.J. Sonntag, T.A.S. Kaufmann, U. Steinseifer, F. Nicoud, Fluid-structure interaction of a pulsatile flow with an aortic valve model: a combined experimental and numerical study, Int. J. Numer. Method. Biomed. Eng. 34 (2018), https://doi.org/10.1002/cnm.2945.

[31] A.M. Tango, A. Ducci, G. Burriesci, In silico study of the ageing effect upon aortic valves, J. Fluid. Struct. 103 (2021) 103258, https://doi.org/10.1016/j.jfluidstructs.2021.103258.

[32] J. De Hart, G.W.M. Peters, P.J.G. Schreurs, F.P.T. Baaijens, A two-dimensional fluid–structure interaction model of the aortic value, J. Biomech. 33 (2000) 1079–1088, https://doi.org/10.1016/S0021-9290(00)00068-3.

[33] J. De Hart, G.W.M. Peters, P.J.G. Schreurs, F.P.T. Baaijens, A three-dimensional computational analysis of fluid–structure interaction in the aortic valve, J. Biomech. 36 (2003) 103–112, https://doi.org/10.1016/S0021-9290(02)00244-0.

[34] M.-C. Hsu, D. Kamensky, Y. Bazilevs, M.S. Sacks, T.J.R. Hughes, Fluid–structure interaction analysis of bioprosthetic heart valves: significance of arterial wall deformation, Comput. Mech. 54 (2014) 1055–1071, https://doi.org/10.1007/s00466-014-1059-4.

[35] A. Khayyer, H. Gotoh, Y. Shimizu, On systematic development of FSI solvers in the context of particle methods, J. Hydrodyn. 34 (2022) 395–407, https://doi.org/10.1007/s42241-022-0042-3.

[36] P.B. Ryzhakov, R. Rossi, S.R. Idelsohn, E. Oñate, A monolithic Lagrangian approach for fluid–structure interaction problems, Comput. Mech. 46 (2010) 883–899, https://doi.org/10.1007/s00466-010-0522-0.

[37] A. Franci, E. Oñate, J.M. Carbonell, Unified Lagrangian formulation for solid and fluid mechanics and FSI problems, Comput. Method. Appl. Mech. Eng. 298 (2016) 520–547, https://doi.org/10.1016/j.cma.2015.09.023.

[38] M.L. Cerquaglia, D. Thomas, R. Boman, V. Terrapon, J.-P. Ponthot, A fully partitioned Lagrangian framework for FSI problems characterized by free surfaces, large solid deformations and displacements, and strong added-mass effects, Comput. Method. Appl. Mech. Eng. 348 (2019) 409–442, https://doi.org/10.1016/j.cma.2019.01.021.

[39] T. Rabczuk, R. Gracie, J.-H. Song, T. Belytschko, Immersed particle method for fluid-structure interaction, Int. J. Numer. Method. Eng. 81 (2010) 48–71, https://doi.org/10.1002/nme.2670.

[40] Z. Sun, K. Djidjeli, J.T. Xing, F. cheng, Modified MPS method for the 2D fluid structure interaction problem with free surface, Comput. Fluid. 122 (2015) 47–65, https://doi.org/10.1016/j.compfluid.2015.08.017.

[41] Y. Sun, G. Xi, Z. Sun, A fully Lagrangian method for fluid–structure interaction problems with deformable floating structure, J. Fluids. Struct. 90 (2019) 379–395, https://doi.org/10.1016/j.jfluidstructs.2019.07.005.

[42] L.B. Lucy, A numerical approach to the testing of the fission hypothesis, Astron. J. 82 (1977) 1013, https://doi.org/10.1086/112164.

[43] R.A. Gingold, J.J. Monaghan, Smoothed particle hydrodynamics: theory and application to non-spherical stars, Mon. Not. R. Astron. Soc. 181 (1977) 375–389, https://doi.org/10.1093/mnras/181.3.375.

[44] M.B. Liu, G.R. Liu, Smoothed particle hydrodynamics (SPH): an overview and recent developments, Arch. Comput. Method. Eng. 17 (2010) 25–76, https://doi.org/10.1007/s11831-010-9040-7.
[45] J.J. Monaghan, Smoothed particle hydrodynamics and its diverse applications, Annu. Rev. Fluid. Mech. 44 (2012) 323–346, https://doi.org/10.1146/annurev-fluid-120710-101220.
[46] A. Zhang, P. Sun, F. Ming, A. Colagrossi, Smoothed particle hydrodynamics and its applications in fluid-structure interactions, J. Hydrodyn. 29 (2017) 187–216, https://doi.org/10.1016/S1001-6058(16)60730-8.
[47] M. Liu, Z. Zhang, Smoothed particle hydrodynamics (SPH) for modeling fluid-structure interactions, Sci. China Phys. Mech. Astron. 62 (2019) 984701, https://doi.org/10.1007/s11433-018-9357-0.
[48] T. De Vuyst, R. Vignjevic, J.C. Campbell, Coupling between meshless and finite element methods, Int. J. Impact. Eng. 31 (2005) 1054–1064, https://doi.org/10.1016/j.ijimpeng.2004.04.017.
[49] G. Fourey, C. Hermange, D.Le Touzé, G. Oger, An efficient FSI coupling strategy between smoothed particle hydrodynamics and finite element methods, Comput. Phys. Commun. 217 (2017) 66–81, https://doi.org/10.1016/j.cpc.2017.04.005.
[50] T. Long, D. Hu, D. Wan, C. Zhuang, G. Yang, An arbitrary boundary with ghost particles incorporated in coupled FEM–SPH model for FSI problems, J. Comput. Phys. 350 (2017) 166–183, https://doi.org/10.1016/j.jcp.2017.08.044.
[51] S.L. Fuchs, C. Meier, W.A. Wall, C.J. Cyron, A novel smoothed particle hydrodynamics and finite element coupling scheme for fluid–structure interaction: the sliding boundary particle approach, Comput. Methods Appl. Mech. Eng. 383 (2021) 113922, https://doi.org/10.1016/j.cma.2021.113922.
[52] Y. Dabiri, J. Yao, K.L. Sack, G.S. Kassab, J.M. Guccione, Tricuspid valve regurgitation decreases after mitraclip implantation: fluid structure interaction simulation, Mech. Res. Commun. 97 (2019) 96–100, https://doi.org/10.1016/j.mechrescom.2019.04.009.
[53] M. McLoone, N.J. Quinlan, Coupling of the meshless finite volume particle method and the finite element method for fluid–structure interaction with thin elastic structures, Eur. J. Mech. - B/Fluid. 92 (2022) 117–131, https://doi.org/10.1016/j.euromechflu.2021.12.001.
[54] S.M. Hosseini, J.J. Feng, A particle-based model for the transport of erythrocytes in capillaries, Chem. Eng. Sci. 64 (2009) 4488–4497, https://doi.org/10.1016/j.ces.2008.11.028.
[55] X. Yang, M. Liu, S. Peng, C. Huang, Numerical modeling of dam-break flow impacting on flexible structures using an improved SPH–EBG method, Coast. Eng. 108 (2016) 56–64, https://doi.org/10.1016/j.coastaleng.2015.11.007.
[56] Z.L. Zhang, T. Long, J.Z. Chang, M.B. Liu, A smoothed particle element method (SPEM) for modeling fluid–structure interaction problems with large fluid deformations, Comput. Method. Appl. Mech. Eng. 356 (2019) 261–293, https://doi.org/10.1016/j.cma.2019.07.024.
[57] Z. Zhang, C. Shu, Y. Liu, W. Liu, M.S.U. Khalid, An improved M-SPEM for modeling complex hydroelastic fluid-structure interaction problems, J. Comput. Phys. 488 (2023) 112233, https://doi.org/10.1016/j.jcp.2023.112233.
[58] Y. Shimizu, A. Khayyer, H. Gotoh, An implicit SPH-based structure model for accurate fluid–structure interaction simulations with hourglass control scheme, Eur. J. Mech. - B/Fluid. 96 (2022) 122–145, https://doi.org/10.1016/j.euromechflu.2022.07.007.
[59] G. Zhang, S. Wang, Z. Sui, L. Sun, Z. Zhang, Z. Zong, Coupling of SPH with smoothed point interpolation method for violent fluid-structure interaction problems, Eng. Anal. Bound. Elem. 103 (2019) 1–10, https://doi.org/10.1016/j.enganabound.2019.02.010.
[60] G. Zhang, T. Hu, Z. Sun, S. Wang, S. Shi, Z. Zhang, A δSPH–SPIM coupled method for fluid–structure interaction problems, J. Fluid. Struct. 101 (2021) 103210, https://doi.org/10.1016/j.jfluidstructs.2020.103210.
[61] M.N. Rahimi, D.C. Kolukisa, M. Yildiz, M. Ozbulut, A. Kefal, A generalized hybrid smoothed particle hydrodynamics–peridynamics algorithm with a novel Lagrangian mapping for solution and failure analysis of fluid–structure interaction problems, Comput. Method. Appl. Mech. Eng. 389 (2022) 114370, https://doi.org/10.1016/j.cma.2021.114370.
[62] M.K. Rausch, G.E. Karniadakis, J.D. Humphrey, Modeling soft tissue damage and failure using a combined particle/continuum approach, Biomech. Model. Mechanobiol. 16 (2017) 249–261, https://doi.org/10.1007/s10237-016-0814-1.
[63] H. Naceur, J. Lin, D. Coutellier, A. Laksimi, Efficient smoothed particle hydrodynamics method for the analysis of planar structures undergoing geometric nonlinearities, J. Mech. Sci. Technol. 29 (2015) 2147–2155, https://doi.org/10.1007/s12206-015-0232-9.
[64] È. Lluch, M. de Craene, B. Bijnens, M. Sermesant, J. Noailly, O. Camara, H. G. Morales, Breaking the state of the heart: meshless model for cardiac mechanics, Biomech. Model. Mechanobiol. 18 (2019) 1549–1561, https://doi.org/10.1007/s10237-019-01175-9.
[65] C. Antoci, M. Gallati, S. Sibilla, Numerical simulation of fluid–structure interaction by SPH, Comput. Struct. 85 (2007) 879–890, https://doi.org/10.1016/j.compstruc.2007.01.002.
[66] C. Zhang, M. Rezavand, X. Hu, A multi-resolution SPH method for fluid-structure interactions, J. Comput. Phys. 429 (2021) 110028, https://doi.org/10.1016/j.jcp.2020.110028.
[67] A. Rafiee, K.P. Thiagarajan, An SPH projection method for simulating fluid-hypoelastic structure interaction, Comput. Method. Appl. Mech. Eng. 198 (2009) 2785–2795, https://doi.org/10.1016/j.cma.2009.04.001.
[68] A. Khayyer, H. Gotoh, H. Falahaty, Y. Shimizu, An enhanced ISPH–SPH coupled method for simulation of incompressible fluid–elastic structure interactions, Comput. Phys. Commun. 232 (2018) 139–164, https://doi.org/10.1016/j.cpc.2018.05.012.
[69] L. Zhan, C. Peng, B. Zhang, W. Wu, A stabilized TL–WC SPH approach with GPU acceleration for three-dimensional fluid–structure interaction, J. Fluid. Struct. 86 (2019) 329–353, https://doi.org/10.1016/j.jfluidstructs.2019.02.002.
[70] A. Khayyer, Y. Shimizu, H. Gotoh, K. Nagashima, A coupled incompressible SPH-Hamiltonian SPH solver for hydroelastic FSI corresponding to composite structures, Appl Math Model 94 (2021) 242–271, https://doi.org/10.1016/j.apm.2021.01.011.
[71] P.-N. Sun, D.Le Touzé, G. Oger, A.-M. Zhang, An accurate FSI-SPH modeling of challenging fluid-structure interaction problems in two and three dimensions, Ocean Eng. 221 (2021) 108552, https://doi.org/10.1016/j.oceaneng.2020.108552.
[72] J. O'Connor, B.D. Rogers, A fluid–structure interaction model for free-surface flows and flexible structures using smoothed particle hydrodynamics on a GPU, J. Fluid. Struct. 104 (2021) 103312, https://doi.org/10.1016/j.jfluidstructs.2021.103312.
[73] K. Wu, D. Yang, N. Wright, A coupled SPH-DEM model for fluid-structure interaction problems with free-surface flow and structural failure, Comput. Struct. 177 (2016) 141–161, https://doi.org/10.1016/j.compstruc.2016.08.012.
[74] H. Tan, S. Chen, A hybrid DEM-SPH model for deformable landslide and its generated surge waves, Adv. Water. Resour. 108 (2017) 256–276, https://doi.org/10.1016/j.advwatres.2017.07.023.
[75] M. Ariane, D. Vigolo, A. Brill, F.G.B. Nash, M. Barigou, A. Alexiadis, Using discrete multi-physics for studying the dynamics of emboli in flexible venous valves, Comput. Fluid. 166 (2018) 57–63, https://doi.org/10.1016/j.compfluid.2018.01.037.
[76] Z. Pan, R. Ma, D. Wang, A. Chen, A review of lattice type model in fracture mechanics: theory, applications, and perspectives, Eng. Fract. Mech. 190 (2018) 382–409, https://doi.org/10.1016/j.engfracmech.2017.12.037.
[77] K.C. Ng, A. Alexiadis, H. Chen, T.W.H. Sheu, A coupled smoothed particle hydrodynamics-volume compensated particle method (SPH-VCPM) for fluid structure interaction (FSI) modelling, Ocean Eng. 218 (2020) 107923, https://doi.org/10.1016/j.oceaneng.2020.107923.
[78] K.C. Ng, A. Alexiadis, H. Chen, T.W.H. Sheu, Numerical computation of fluid–solid mixture flow using the SPH–VCPM–DEM method, J. Fluid. Struct. 106 (2021) 103369, https://doi.org/10.1016/j.jfluidstructs.2021.103369.
[79] K.C. Ng, A. Alexiadis, Y.L. Ng, An improved particle method for simulating fluid-structure interactions: the multi-resolution SPH-VCPM approach, Ocean Eng. 247 (2022) 110779, https://doi.org/10.1016/j.oceaneng.2022.110779.
[80] K.C. Ng, W.C. Low, H. Chen, A. Tafuni, A. Nakayama, A three-dimensional fluid-structure interaction model based on SPH and lattice-spring method for simulating complex hydroelastic problems, Ocean Eng. 260 (2022) 112026, https://doi.org/10.1016/j.oceaneng.2022.112026.
[81] W.C. Low, K.C. Ng, H.K. Ng, A SPH-lattice spring method for modelling fluid structure interaction involving composite body and free surface, Comput. Part Mech. 10 (2023) 1587–1612, https://doi.org/10.1007/s40571-023-00576-z.
[82] A. Monteleone, G. Borino, E. Napoli, G. Burriesci, Fluid–structure interaction approach with smoothed particle hydrodynamics and particle–spring systems, Comput. Methods Appl. Mech. Eng. 392 (2022) 114728, https://doi.org/10.1016/j.cma.2022.114728.
[83] E. Napoli, M. De Marchis, E. Vitanza, PANORMUS-SPH. A new smoothed particle hydrodynamics solver for incompressible flows, Comput. Fluids. 106 (2015) 185–195, https://doi.org/10.1016/j.compfluid.2014.09.045.
[84] R. Gnyaneshwar, R.K. Kumar, K.R. Balakrishnan, Dynamic analysis of the aortic valve using a finite element model, Ann. Thorac. Surg. 73 (2002) 1122–1129, https://doi.org/10.1016/S0003-4975(01)03588-3.
[85] L.R. Croft, M.R. Kaazempur Mofrad, Computational Modeling in Biomechanics, Springer, Netherlands, Dordrecht, 2010, https://doi.org/10.1007/978-90-481-3575-2.
[86] T. Ishihara, V.J. Ferrans, M. Jones, S.W. Boyce, O. Kawanami, W.C. Roberts, Histologic and ultrastructural features of normal human parietal pericardium, Am. J. Cardiol. 46 (1980) 744–753, https://doi.org/10.1016/0002-9149(80)90424-5.
[87] F. Di Puccio, S. Celi, P. Forte, Review of experimental investigations on compressibility of arteries and introduction of a new apparatus, Exp. Mech. 52 (2012) 895–902, https://doi.org/10.1007/s11340-012-9614-4.
[88] Y.C. Fung, Biomechanics: Mechanical Properties of Living Tissues, Springer Verlag, New York, 1993.
[89] H. Wendland, Piecewise polynomial, positive definite and compactly supported radial functions of minimal degree, Adv. Comput. Math. 4 (1995) 389–396, https://doi.org/10.1007/BF02123482.
[90] E. Napoli, M. De Marchis, C. Gianguzzi, B. Milici, A. Monteleone, A coupled Finite Volume–Smoothed Particle Hydrodynamics method for incompressible flows, Comput. Methods Appl. Mech. Eng. 310 (2016) 674–693, https://doi.org/10.1016/j.cma.2016.07.034.
[91] A. Monteleone, M. De Marchis, B. Milici, E. Napoli, A multi-domain approach for smoothed particle hydrodynamics simulations of highly complex flows, Comput. Methods Appl. Mech. Eng. 340 (2018) 956–977, https://doi.org/10.1016/j.cma.2018.06.029.
[92] A. Monteleone, M. Monteforte, E. Napoli, Inflow/outflow pressure boundary conditions for smoothed particle hydrodynamics simulations of incompressible flows, Comput. Fluids. 159 (2017), https://doi.org/10.1016/j.compfluid.2017.09.011.
[93] A.J. Chorin, Numerical solution of the Navier-Stokes equations, Math. Comput. 22 (1968) 745–762, https://doi.org/10.1090/S0025-5718-1968-0242392-2.
[94] E. Hairer, S. Nørset, G. Wanner. Solving Ordinary Differential Equations I, Springer Berlin, 1993, https://doi.org/10.1007/978-3-540-78862-1.

[95] H.A. van der Vorst, Bi-CGSTAB: a fast and smoothly converging variant of Bi-CG for the solution of nonsymmetric linear systems, SIAM J. Sci. Statist. Comput. 13 (1992) 631–644, https://doi.org/10.1137/0913035.
[96] Y. Saad, Iterative Methods for Sparse Linear Systems, 2003.
[97] J.W. Swegle, D.L. Hicks, S.W. Attaway, Smoothed particle hydrodynamics stability analysis, J. Comput. Phys. 116 (1995) 123–134, https://doi.org/10.1006/jcph.1995.1010.
[98] R. Xu, P. Stansby, D. Laurence, Accuracy and stability in incompressible SPH (ISPH) based on the projection method and a new approach, J. Comput. Phys. 228 (2009) 6703–6725, https://doi.org/10.1016/j.jcp.2009.05.032.
[99] A. Monteleone, A. Viola, E. Napoli, G. Burriesci, Modelling of thrombus formation using smoothed particle hydrodynamics method, PLoS One 18 (2023) e0281424, https://doi.org/10.1371/journal.pone.0281424.
[100] S.K. Chimakurthi, S. Reuss, M. Tooley, S. Scampoli, ANSYS workbench system coupling: a state-of-the-art computational framework for analyzing multiphysics problems, Eng. Comput. 34 (2018) 385–411, https://doi.org/10.1007/s00366-017-0548-4.
[101] A. Monteleone, G. Burriesci, E. Napoli, A distributed-memory MPI parallelization scheme for multi-domain incompressible SPH, J. Parallel. Distrib. Comput. 170 (2022) 53–67, https://doi.org/10.1016/j.jpdc.2022.08.004.
[102] V.T. Nkomo, J.M. Gardin, T.N. Skelton, J.S. Gottdiener, C.G. Scott, M. Enriquez-Sarano, Burden of valvular heart diseases: a population-based study, Lancet 368 (2006) 1005–1011, https://doi.org/10.1016/S0140-6736(06)69208-8.
[103] A.M. Tango, J. Salmonsmith, A. Ducci, G. Burriesci, Validation and extension of a fluid–structure interaction model of the healthy aortic valve, Cardiovasc. Eng. Technol. 9 (2018) 739–751, https://doi.org/10.1007/s13239-018-00391-1.
[104] M. Thubrikar, The Aortic Valve, 1990. Boca Raton.
[105] R. van Loon, P.D. Anderson, F.N. van de Vosse, A fluid–structure interaction method with solid-rigid contact for heart valve dynamics, J. Comput. Phys. 217 (2006) 806–823, https://doi.org/10.1016/j.jcp.2006.01.032.
[106] G. Musotto, A. Monteleone, D. Vella, S. Di Leonardo, A. Viola, G. Pitarresi, B. Zuccarello, A. Pantano, A. Cook, G.M. Bosi, G. Burriesci, The role of patient-specific morphological features of the left atrial appendage on the thromboembolic risk under atrial fibrillation, Front. Cardiovasc. Med. 9 (2022), https://doi.org/10.3389/fcvm.2022.894187.
[107] D. Vella, A. Monteleone, G. Musotto, G.M.G.M. Bosi, G. Burriesci, Effect of the alterations in contractility and morphology produced by atrial fibrillation on the thrombosis potential of the left atrial appendage, Front. Bioeng. Biotechnol. 9 (2021) 147, https://doi.org/10.3389/fbioe.2021.586041.
[108] Y.C. Fung, S.C. Cowin, Biomechanics: mechanical properties of living tissues, 2nd ed. J. Appl. Mech. 61 (1994) 1007, https://doi.org/10.1115/1.2901550. –1007
[109] F.J. Schoen, R.J. Levy, Tissue heart valves: current challenges and future research perspectives, J. Biomed. Mater. Res. 47 (1999) 439–465, https://doi.org/10.1002/(SICI)1097-4636(19991215)47, 4<439::AID−JBM1>3.0.CO;2-O.
[110] M. Misfeld, H.-H. Sievers, Heart valve macro- and microstructure, Philosoph. Transact. Roy. Soc. B: Biolog. Sci. 362 (2007) 1421–1436, https://doi.org/10.1098/rstb.2007.2125.
[111] A. Hasan, K. Ragaert, W. Swieszkowski, Š. Selimović, A. Paul, G. Camci-Unal, M. R.K. Mofrad, A. Khademhosseini, Biomechanical properties of native and tissue engineered heart valve constructs, J. Biomech. 47 (2014) 1949–1963, https://doi.org/10.1016/j.jbiomech.2013.09.023.
[112] L. R.M. C. D. Wiltz, C. Alexander, A.A. Blancas, X. Zhang, K. Jane, Extracellular matrix organization, structure, and function. Calcific Aortic Valve Disease, InTech, 2013, https://doi.org/10.5772/52842.
[113] A. Cataloglu, R.E. Clark, P.L. Gould, Stress analysis of aortic valve leaflets with smoothed geometrical data, J. Biomech. 10 (1977) 153–158, https://doi.org/10.1016/0021-9290(77)90053-7.
[114] D. Mavrilas, Y. Missirlis, An approach to the optimization of preparation of bioprosthetic heart valves, J. Biomech. 24 (1991) 331–339, https://doi.org/10.1016/0021-9290(91)90351-M.
[115] S. Bozkurt, G.L. Preston-Maher, R. Torii, G. Burriesci, Design, analysis and testing of a novel mitral valve for transcatheter implantation, Ann. Biomed. Eng. 45 (2017) 1852–1864, https://doi.org/10.1007/s10439-017-1828-2.
[116] I. Standard, ISO 5840: Cardiovascular Implants — Cardiac Valve Prostheses, 2021.
[117] S. Di Leonardo, D. Vella, C.S. Grillo, C. Martorana, S. Torre, V. Argano, G. Burriesci, Hydrodynamic ex vivo analysis of valve-sparing techniques: assessment and comparison, Eur. J. Cardio-Thoracic Surg. 63 (2023), https://doi.org/10.1093/ejcts/ezad040.
[118] A. Khayyer, Y. Shimizu, H. Gotoh, S. Hattori, A 3D SPH-based entirely Lagrangian meshfree hydroelastic FSI solver for anisotropic composite structures, Appl. Math. Model. 112 (2022) 560–613, https://doi.org/10.1016/j.apm.2022.07.031.